
AN EMPIRICAL INVESTIGATION OF 3D ANOMALY DETECTION AND SEGMENTATION

Eliahu Horwitz, Yedid Hoshen

School of Computer Science and Engineering
The Hebrew University of Jerusalem, Israel

http://www.vision.huji.ac.il/3d_ads/

{eliahu.horwitz, yedid.hoshen}@mail.huji.ac.il

ABSTRACT

Anomaly detection and segmentation in images has made tremendous progress in recent years while 3D information has often been ignored. The objective of this paper is to further understand the benefit and role of 3D as opposed to color in image anomaly detection. Our study begins by presenting a surprising finding: standard color-only anomaly segmentation methods, when applied to 3D datasets, significantly outperform all current methods. On the other hand, we observe that color-only methods are insufficient for images containing geometric anomalies where shape cannot be unambiguously inferred from 2D. This suggests that better 3D methods are needed. We investigate different representations for 3D anomaly detection and discover that handcrafted orientation-invariant representations are unreasonably effective on this task. We uncover a simple 3D-only method that outperforms all recent approaches while not using deep learning, external pretraining datasets, or color information. As the 3D-only method cannot detect color and texture anomalies, we combine it with 2D color features, granting us the best current results by a large margin (Pixel-wise ROCAUC: 99.2%, PRO: 95.9% on MVTec 3D-AD). We conclude by discussing future challenges for 3D anomaly detection and segmentation.

1 Introduction

Image anomaly detection seeks to identify patterns in images that significantly deviate from the norm while anomaly segmentation localizes anomalies within anomalous images. These tasks have important applications (e.g. manufacturing defect detection [2] and identifying new biomarkers in medical images [37].) The field has seen tremendous progress in recent years, accelerated by advancements in representation learning and the introduction of the widely used MVTec AD [2] benchmark. Current state-of-the-art methods (e.g. SPADE, PatchCore [9, 33]) extract representations of local image regions and score the regions as normal or anomalous using the estimated probability density of the representation. These methods virtually solve the MVTec AD dataset with PatchCore achieving ROCAUC score of 99.1% for anomalous image detection and 98.1% for pixel-wise segmentation. While shape information is fundamental to computer vision, it has typically not been considered by current anomaly detection and segmentation approaches, probably due to the lack of suitable datasets. Recently, the MVTec 3D-AD [4] dataset was introduced in order to encourage research into 3D anomaly detection and segmentation (AD&S). To address the gap between 2D and 3D AD&S, we conduct an empirical investigation on the MVTec 3D-AD which seeks the answers to several questions:

1. Are current 3D methods outperforming state-of-the-art 2D AD&S methods?
2. Is 3D information *potentially* useful for AD&S?
3. What are effective ways of representing 3D local regions for AD&S?
4. Are there complementary benefits from using both 3D and color features?

Our investigation begins by examining if current AD&S are indeed benefiting from 3D information. Perhaps surprisingly, we find that standard 2D methods (particularly PatchCore [33]) using RGB-only information, outperform

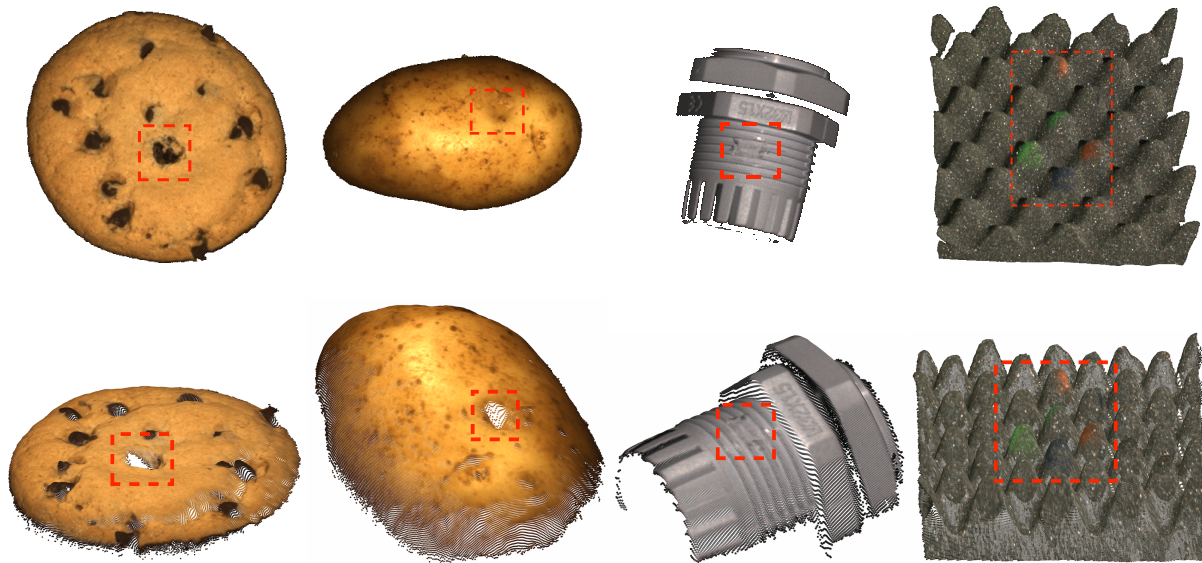


Figure 1: **RGB vs. 3D**: Top: Anomalous images using the RGB-only image. Bottom: The same image is viewed from different angles, enabled by the 3D information. The cookie and potato exhibit geometric anomalies while the cable gland and foam contain RGB anomalies. Cookie: The hole blends in with the rest of the chocolate chips. Potato: The dent goes undetected when viewed from above. Cable Gland: The deformed texture is hard to tell apart by examining the geometry alone. Foam: The colors can not be inferred by relying solely on 3D cues.

all current methods by a wide margin. We also investigate whether 3D information is needed *at all* for AD&S. Encouragingly, we find that several types of anomalies are not easy to detect using 2D-only methods, motivating the development of better 3D methods. We present several examples of such cases in the left half of Fig. 1-top row, the anomaly in each object cannot be detected from color information only. In the bottom row we present another view of the same objects where the anomalies are easily detected. This motivates using 3D information for AD&S.

We conduct an extensive empirical investigation of representations for AD&S based on 3D data. Guidance is provided by 2D AD&S methods, where the best results are obtained by using simple anomaly detection methods on strong local region feature representations. Our investigation examines a large range of approaches including handcrafted descriptors and pre-trained deep features for both depth and 3D approaches. Our surprising result is that a classical 3D handcrafted point cloud descriptor outperforms all other 3D methods - including all previously presented baselines as well as a concurrent deep-learning-based point cloud approach. Furthermore, these features outperform the state-of-the-art 2D color approaches (particularly PatchCore). The main insight is that 3D surface matching approaches are highly effective for 3D AD&S tasks. Finally, we note that for several categories, anomalies cannot be detected solely using geometric cues. We therefore investigate whether geometric and color features hold complimentary benefits. Our best investigated approach combines 3D and color to achieve the best recorded result on the MVTEC 3D-AD dataset by a very wide margin (99.2% *Pixel-wise ROCAUC*, 95.9% *PRO*, and 86.5% *Image ROCAUC*).

To summarize, our main contributions in this paper are:

- Conducting a thorough analysis of the important and unexplored field of anomaly detection and segmentation for images with color and 3D information.
- Identifying significant gaps in today’s current state-of-the-art 3D-based methods.
- The discovery of highly effective 3D AD&S methods with connections to surface matching.
- Proposing a combination of the handcrafted 3D method with the current state-of-the-art 2D color-based method, outperforming current state-of-the-art by a wide margin.

2 Related Work

Anomaly detection and segmentation. Anomaly detection methods have been researched for several decades, most approaches are based either on density estimation or out-of-domain generalization ideas. Classical approaches include:

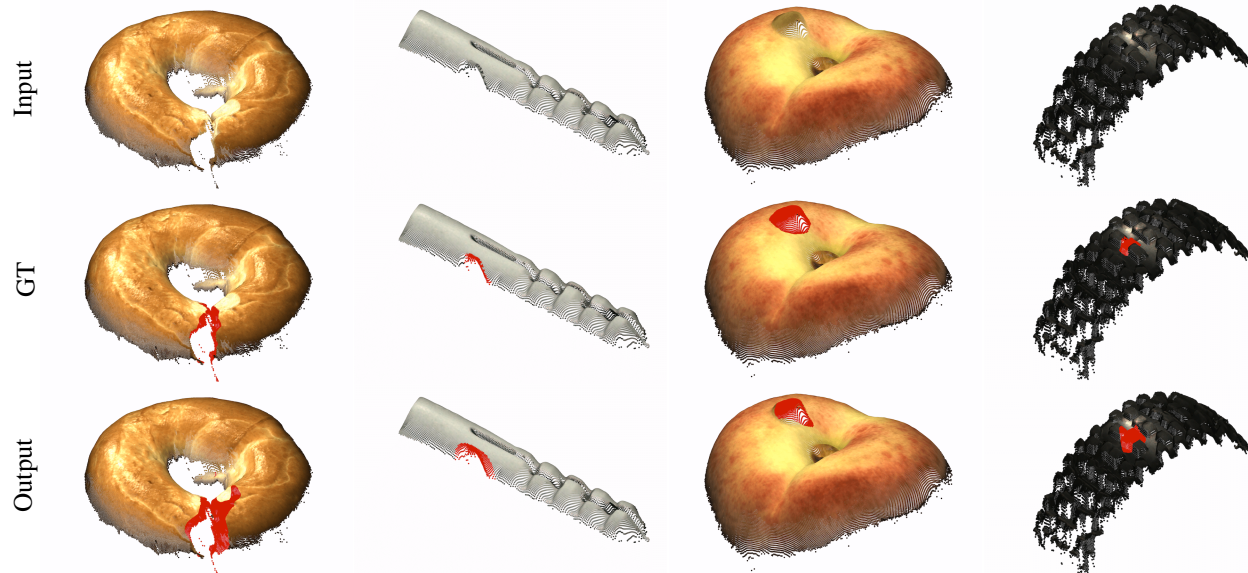


Figure 2: **Additional Results:** RGB + FPFH method is used. All anomalies are correctly segmented (marked in red).

k-Nearest-Neighbors (kNN) [14], KDE [25], GMM [18], PCA [23], one class SVM (OCSVM) [39], and isolation forests [27]. With the advent of deep learning, these methods were extended with deep representations including: DAGMM [48] extending PCA, and DeepSVDD [34] extending OCSVM. A novel line of work extends self-supervised approaches to anomaly detection, including Golan and El-Yaniv [19], and Hendrycks et al. [22] that extend RotNet [17] and CSI [43] who extend contrastive methods [20, 21, 8]. We follow another line of works that assumes the availability of pre-trained representations, and combines them with a kNN scoring function. Such works include Perera and Patel [29], and PANDA [31]. These works have been extended to anomaly segmentation including SPADE [9], PADIM [12] and PatchCore [33]. Very recent works have used more advanced density estimation models on the extracted representation, an example is FastFlow [45]. Other approaches for anomaly segmentation include Student-Teacher autoencoder approaches [3] as well as self-supervised methods that synthesize anomalies such as CutPaste [26] and NSA [38].

Anomaly detection and segmentation with 3D information. In contrast to the large amount of research on 2D anomaly detection approaches, 3D anomaly detection has not been extensively researched. In medical imaging research, work was performed to adapt anomaly detection methods to voxel data. Simarro et al. [41] extend f-Anogan [37, 36] to 3D. Bengs et al. [1] presented a 3D autoencoder approach for medical voxel data. Voxel data is significantly different from point cloud 3D data. Bergmann et al. [4] recognized that a dataset for anomaly segmentation in 3D point cloud data is missing and introduced MVTEC 3D-AD. We expect this to be a critical contribution to the development of 3D anomaly detection and segmentation. Concurrently to our work, Bergmann and Sattlegger [5] introduced a 3D point cloud based approach dubbed $3D - ST_{128}$ for anomaly detection, we include this work in our investigation.

3 AD&S Formulation

The setting in this paper assumes a set of input training samples x_1, x_2, \dots, x_N that are all normal. At test time, we are given a test sample y . The task of anomaly detection is to learn a sample-level scoring function σ_d , such that $\sigma_d(y) > 0$ if the sample is anomalous and $\sigma_d(y) \leq 0$ if the sample is normal. The task of anomaly segmentation is to learn a pixel-level scoring function σ_s , which satisfies $\sigma_s(y, i) > 0$ if pixel i of sample y is anomalous, and $\sigma_s(y, i) \leq 0$ if it is normal. Note that a sample can be an RGB image, a depth map (i.e. 1-channel image), an organized or unorganized point cloud, or a pair of these as a tuple. For brevity we use the term "pixel", however, when relevant, it may stand for a point cloud point.

A common pipeline used by state-of-the-art methods (e.g. SPADE [9], PatchCore [33]) consists of two stages: i) Representation extraction of local regions ii) Evaluating the normality of each local representation, for example by using the nearest-neighbor distance to a normal training dataset. The focus of this paper is on the representation stage, particularly, on finding the best representation for AD&S when 3D information is available.

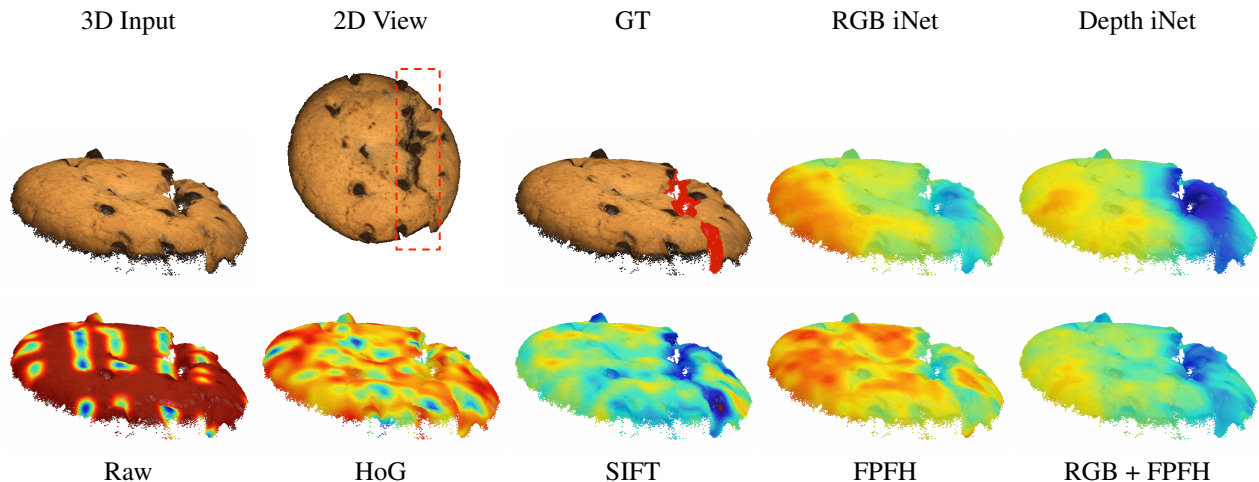


Figure 3: *Anomaly Heatmaps (Pixel-wise)*: For each method, the distances heatmap is shown, *PRO* and *P-ROC* are drawn from these distances. Blue colors are further away (i.e. more anomalous) while red colors are closer (i.e. less anomalous). Ground truth segmentation in red, anomaly indicated by a red rectangle in the 2D view, “iNet” indicates ImageNet pre-trained.

Representation. The first stage computes a representation of each local region. Let us denote each local region of an image by index j , where the region can consist of one or more pixels. The representation function of region j of image x is denoted $\phi(x, j)$. The representation can be learned or be handcrafted. This paper will investigate many different such representations.

Anomaly scoring. Given the representations in every local region j of every training image x , we can train a model $\sigma_s(y, j')$ which computes the likelihood of a new representation $\phi(y, j')$. Although some approaches train parametric models for the density of the representations, non-parametric approaches are much simpler and require no training. Specifically, in our investigation, we use the k -Nearest-Neighbor distance of representation $\phi(y, j')$ to the set of all training set representations $S = \{\phi(x, j) \forall x \forall j\}$. Despite their simplicity, such approaches are very accurate, require no training, and can be significantly sped up using coreset techniques.

3.1 Benchmark

Our investigation uses the recently published MVTEC 3D Anomaly Detection dataset (MVTEC 3D-AD [4]). It contains over 4000 high-resolution 3D scans of industrially manufactured products across 10 categories. Each sample is represented by an *organized* point cloud and a corresponding RGB image with a one-to-one mapping between the pixels in the point cloud and those in the RGB image. Currently, this is the only dataset available for 3D AD&S. Five of the classes in the dataset exhibit natural variations (*bagel*, *carrot*, *cookie*, *peach*, and *potato*). The classes *cable gland* and *dowel* are of rigid bodies, while the classes *foam*, *rope*, and *tire* are “man-made” but deformable. Alongside the dataset, three baselines are introduced i) GAN-based ii) AE-based iii) a classic baseline based on per-pixel mean and standard deviation dubbed the “Variation Model (VM)”. These models operate either on the depth images or in voxel space with additional variants that operate on 3D+RGB information.

3.2 Evaluation Metrics

Several evaluation metrics for AD&S exist. For anomaly detection on the image level, ROCAUC [7] is used, in this paper, we denote it by *I-ROC*. Two metrics exist for anomaly segmentation, both operate on the pixel level. Pixel-wise ROCAUC is an extension of the classic ROCAUC to work on the pixel level by simply treating each pixel in the dataset as a sample and taking the ROCAUC over all pixels in the dataset, we denote it by *P-ROC*.

The PRO [2] metric is defined as the average relative overlap of the binary prediction P with each ground truth connected component C_k . It is measured in a similar way to the *P-ROC* and is simply denoted by *PRO*.

$$\text{PRO} = \frac{1}{K} \sum_{k=1}^K \frac{|P \cap C_k|}{|C_k|}, \quad (1)$$

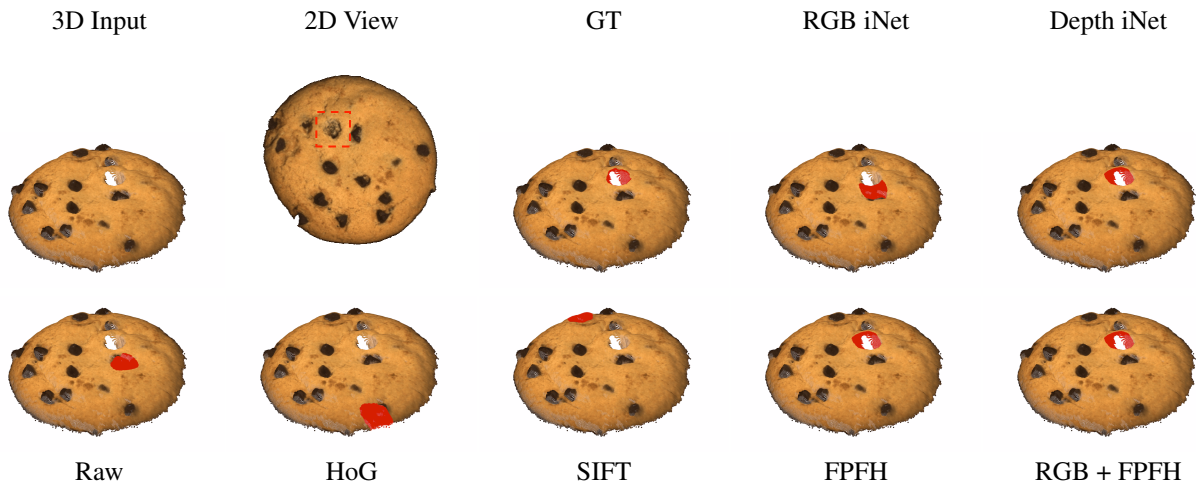


Figure 4: **Most Distant Patch (I-ROC)**: The patch with the largest kNN distance is shown in red for each representation. Anomaly indicated by a red square in the 2D view, "iNet" indicates ImageNet pre-trained.

Table 1: **MVTec Baselines vs. 2D RGB (PRO/I-ROC)**: Average metrics across all classes, best performing MVTEC 3D-AD baselines are shown

Voxel GAN	Voxel + RGB GAN	Point Cloud 3D - ST_{128}	RGB PatchCore
0.583/0.537	0.639/0.517	0.833/-	0.876/0.770

Where K denotes the number of ground truth components. The final metric is computed by integrating this curve up to some false positive rate and normalizing. It is common practice to report *PRO* on an integration limit of at most 0.3, unless otherwise stated, all *PRO* figures reported in this paper use this integration limit.

4 An Empirical Investigation of 3D AD&S

4.1 Examining Current 3D vs. 2D Methods for AD&S

We begin our investigation by answering the question: "How effective are current 3D methods over the state-of-the-art 2D methods?". To represent 3D methods, we test two approaches: i) Voxel GAN [4], a generative method proposed as a baseline for 3D AD&S. While it has several variants, we use the best performing ones, which are "Voxel" and "Voxel + RGB". ii) 3D-ST [6], a concurrent method that uses a point cloud student-teacher model to learn meaningful 3D representations. We use PatchCore [33] to represent color-based 2D AD&S methods. Importantly, PatchCore uses features that were pre-trained on the ImageNet [13] dataset, which have been shown to be highly effective for AD&S, in contrast, 3D-ST used ModelNet10 [44] for pretraining the teacher model. The results on MVTEC 3D-AD are presented in Tab. 1. In accordance with previous work, we report the *PRO* metric with integration limits of 0.3. Surprisingly, PatchCore, which does not use 3D information, outperforms all other methods.

Conclusion. Current methods that use 3D or 3D + color information do not outperform current state-of-the-art methods that use only 2D color information but not 3D.

4.2 Inspecting the Utility of 3D Information for AD&S

Provided the negative results of Sec. 4.1, we are faced with a second question: "Is 3D information *potentially* useful for AD&S?". Although we do not give a definite answer to this question, we motivate the reason as to why the answer may be affirmative.

Ambiguous geometry. Frequently, the geometry of an underlying object cannot be unambiguously determined by observing the 2D RGB image exclusively. In such cases, observing the three-dimensional shape of the object may

Table 2: *Summary of Our Findings*: Average metrics across all classes, "iNet" indicates ImageNet pre-trained, PC for Point Cloud

	RGB iNet	Depth iNet	Depth NSA	Depth Raw	Depth HoG	Depth SIFT	PC FPFH	RGB + PC RGB + FPFH
PRO	0.876	0.755	0.572	0.442	0.771	0.910	0.924	0.959
I-ROC	0.770	0.675	0.696	0.573	0.559	0.727	0.782	0.865
P-ROC	0.967	0.930	0.817	0.771	0.930	0.974	0.978	0.992

Table 3: *MVTec Baselines vs. Raw (PRO)*: Average metrics across all classes, all models use the depth representation

	GAN	AE	VM	Raw
	0.143	0.203	0.374	0.442

reveal the true geometry where the 2D image could not. Two such examples are illustrated in the left half of Fig. 1. The top row contains RGB-only images, in the bottom row, different views of the same object are displayed, revealing the actual geometry and unmasking the anomaly. In the case of the cookie, the hole blends in with the rest of the chocolate chips, making it hard to visually identify the image as anomalous. Using the 3D information to view the object from a different angle makes it easy to spot the anomaly. In the potato case, when looking at the image, it is hard to infer the geometry of the dent from shadow and texture. However, when viewing the potato from different angles, the different texture reveals the dent.

Background variation. While curated datasets often contain synthetic conditions with an object centered in the frame and a clean background, the reality is seldom as simple. Real images contain background which is highly varying but which methods may consider anomalous and therefore trigger false positive alerts. Although background segmentation is not trivial in 2D, it is far easier when the 3D structure is provided. Particularly, the MVTec 3D-AD dataset contains test images with backgrounds that deviate from those of normal data. Such an example is demonstrated in Fig. 5, the background of some objects contains "wave" like patterns in the fabric, due to the dark background, these issues go undetected.

Conclusion. Some anomalies are detectable using 3D information but are not easily detected using 2D color-only images. It is therefore expected that the addition of 3D information should improve AD&S over just 2D information.

4.3 A Study of 3D-Aware Representations for AD&S

Having shown that 3D is under-utilized by current methods, we now seek to answer a third question: "What are effective ways to represent 3D local regions for 3D AD&S?". Using the 3D information, we distinguish among several categories.

Learning-based Representations. We begin by evaluating approaches that utilize learned features. We adapt the two most popular 2D approaches to 3D data i.e. ImageNet-pre-trained features and self-supervised methods.

Depth-only ImageNet Features. The evaluated approach applies PatchCore directly on depth images. This is motivated by the impressive results of ImageNet-pre-trained features on 2D color images (Sec. 4.1). There is also evidence [31, 9] that ImageNet-pre-trained features are effective on image data which is significantly out-of-distribution to ImageNet.

NSA. A different class of learning-based methods approach AD&S from a generative perspective. CutPaste and NSA [26, 38] are recent works that try to mimic anomalies by pasting image patches at different image locations. Specifically, NSA uses Poisson blending [30] to make these appear more natural.

Results. We can observe in Tab. 2 that ImageNet-pre-trained features significantly outperform NSA on depth images. It is possible that NSA performance can be improved by specific per-class augmentations, however, this requires prior knowledge of anomalies. Both approaches underperform PatchCore on 2D color images.

Handcrafted 2D Representations. A notable difference between depth and RGB information is the simplicity of depth information. Consequently, we hypothesize that a simple, handcrafted descriptor should suffice. The following representations use only the depth information (i.e. the Z channel of the point cloud). Furthermore, they do not require external data or training and are all learning-free.

Raw Depth Values. Here, we test perhaps the simplest possible representation, the raw depth values of a patch comprising the region.

Histogram of Oriented Gradients (HoG). Instead of using absolute depth values, HoG [11] considers image gradients and uses histograms to capture the distribution of gradient orientations in the patch. This is potentially more powerful than raw values as the descriptor encodes the spatial structure of the data while being invariant to small translations. On the other hand, HoG is not invariant to global rotations, a much-desired property for 3D representations. Additionally, the small context of HoG makes it invariant to local geometric changes, however, this is counterproductive to our goal of detecting anomalies - usually manifested as local geometric changes.

Dense Scale-Invariant Feature Transform (D-SIFT). In contrast to HoG, SIFT is rotation, scale, and shift-invariant. Different from HoG, SIFT is rotated to align the most dominant direction to the base orientation. This reduces the rotation ambiguity allowing matches between rotated images. While D-SIFT was originally designed for 2D images, it has been shown suitable for certain 3D use cases and extensions have been proposed for 3D-specific tasks [24, 40].

Results. It is clear from Tab. 3, that even the simplest descriptor (raw) excels over all the baselines in their "Depth-only" variant. We can see in Tab. 2 that HoG significantly boosts the pixel-level accuracy achieving better results than raw and learning-based features. These strong results are obtained despite HoG not being specifically designed for 3D information. Finally, the D-SIFT [28] descriptor is able to surpass all previous results (including HoG) on all three metrics. D-SIFT outperforms even the PatchCore RGB results, which have thus far not been surpassed by depth features.

3D Orientation-Invariant Representations. As orientation-invariant 2D features on depth maps have led to the best performance, it begs the question of whether orientation-invariant 3D features can do better. We therefore investigate a representative method.

Fast Point Feature Histograms (FPFH). FPFH [35] first computes the k-Nearest-Neighboring points to the region center point. It then computes a histogram-based representation as a function of the surface normals and vector distance to the nearest neighbors. The representation consists of the histograms of the surface normal based features. This method is chosen as the representative due to its time-tested excellent performance.

Conclusion. FPFH outperforms all methods that use 2D color, depth or both (Tab. 2). The results show that strong, handcrafted, orientation-invariant 3D representations are extremely effective for AD&S when 3D information is available.

4.4 The Benefits of Combining 3D and Color

Having studied different representations for 3D information we now ask: "Are there complimentary benefits from using both 3D and color features?". To address this question we observe that in some cases, geometry alone may not suffice for detecting anomalies. Two examples are fine-textures and color-based anomalies. E.g. the "cable gland" in Fig. 1-right is slightly scraped. While this anomalous texture is clearly observed in the RGB image, it is virtually impossible to detect with the current resolution of the 3D information. This is even more apparent for the foam example, wherein the anomaly is by its nature one of color only. We can also observe in Tab. 4 that amongst methods discussed thus far, ImageNet-pre-trained RGB features achieve the top results on the cable gland class. This suggests that an exclusive focus on 3D fails to account for anomalies involving fine textures or color changes. Combining 3D and RGB representations is therefore necessary.

A Combined RGB + 3D Approach. In order to cater both to 3D geometry and color, we take a combined RGB + 3D approach. To this end, RGB representations are extracted using the 2D ImageNet-based features method discussed in Sec. 4.1 and 3D representations are extracted using FPFH as discussed in Sec. 4.3. Extending PatchCore, these two representations are concatenated and treated as our RGB + 3D representation.

Results. Compared with the previous best method of combining 3D and RGB ("Voxel GAN + RGB"), this method improves the *PRO* (i.e. anomaly segmentation) metric by 32% and *I-ROC* (i.e. anomaly detection) by 16.6%. As illustrated in Tab. 2, compared to using only 3D, the combination improves on the previously discussed FPFH by 3.5% on the *PRO* metric, 8.3% on *I-ROC*, and achieves a score of 99.2% on *P-ROC*, a 1.4% improvement over FPFH.

Conclusion. It is evident by the results RGB and 3D information are complementary and thus by combining their representations one is able to achieve better results. A class level breakdown for each of the investigated methods can be found in Tab. 4 and 5 as well as in the App. A.

Table 4: **Detailed PRO Results:** Top half are current state-of-the-art, bottom half are methods investigated by us. A large number of our methods outperform all current methods by a wide margin. "iNet" indicates ImageNet pre-trained

Method	Bagel	Cable Gland	Carrot	Cookie	Dowel	Foam	Peach	Potato	Rope	Tire	Mean	
Previous Methods	Voxel GAN	0.440	0.453	0.825	0.755	0.782	0.378	0.639	0.775	0.389	0.583	
	+ RGB	0.664	0.620	0.766	0.740	0.783	0.332	0.582	0.790	0.633	0.639	
	Voxel AE	0.260	0.341	0.581	0.351	0.502	0.234	0.351	0.658	0.015	0.185	0.348
	+ RGB	0.467	0.750	0.808	0.550	0.765	0.473	0.721	0.918	0.019	0.170	0.564
	Voxel VM	0.453	0.343	0.521	0.697	0.680	0.284	0.349	0.634	0.616	0.346	0.492
	+ RGB	0.510	0.331	0.413	0.715	0.680	0.279	0.300	0.507	0.611	0.366	0.471
	Depth GAN	0.111	0.072	0.212	0.174	0.160	0.128	0.003	0.042	0.446	0.075	0.143
	+ RGB	0.421	0.422	0.778	0.696	0.494	0.252	0.285	0.362	0.402	0.631	0.474
	Depth AE	0.147	0.069	0.293	0.217	0.207	0.181	0.164	0.066	0.545	0.142	0.203
	+ RGB	0.432	0.158	0.808	0.491	0.841	0.406	0.262	0.216	0.716	0.478	0.481
	Depth VM	0.280	0.374	0.243	0.526	0.485	0.314	0.199	0.388	0.543	0.385	0.374
	+ RGB	0.388	0.321	0.194	0.570	0.408	0.282	0.244	0.349	0.268	0.331	0.335
$3D - ST_{128}$	0.950	0.483	0.986	0.921	0.905	0.632	0.945	0.988	0.976	0.542	0.833	
Our Findings	RGB iNet	0.901	0.949	0.928	0.877	0.892	0.563	0.904	0.932	0.908	0.906	0.876
	Depth iNet	0.769	0.664	0.887	0.880	0.864	0.269	0.876	0.865	0.852	0.624	0.755
	NSA	0.724	0.228	0.716	0.856	0.320	0.432	0.712	0.655	0.818	0.258	0.572
	Raw	0.401	0.311	0.638	0.498	0.250	0.254	0.527	0.530	0.808	0.201	0.442
	HoG	0.711	0.763	0.931	0.497	0.833	0.502	0.743	0.948	0.916	0.858	0.771
	SIFT	0.942	0.842	0.974	0.896	0.910	0.723	0.944	0.981	0.953	0.929	0.910
	FPFH	0.973	0.879	0.982	0.906	0.892	0.735	0.977	0.982	0.956	0.961	0.924
	RGB+FPFH	0.976	0.969	0.979	0.973	0.933	0.888	0.975	0.981	0.950	0.971	0.959

4.5 Implementation Details

Unless otherwise stated, results in the paper downsample the original point clouds and RGB images to 224. Downsampling the point clouds is done by downsampling the organized point cloud (i.e. image downsampling) with nearest-neighbor interpolation, the RGB images are downsampled using bicubic interpolation. When working with unorganized point clouds, the organized point cloud is reshaped from $n \times m \times 3$ into $n \cdot m \times 3$. For depth images, the Z channel of the organized point cloud is used. We use $28 \cdot 28 = 784$ patches (features) per sample, with varying feature dimensions based on the representations used. If the representation is extracted at a different resolution, average pooling is used to match $28 \cdot 28 = 784$. For method-specific details see App. B.

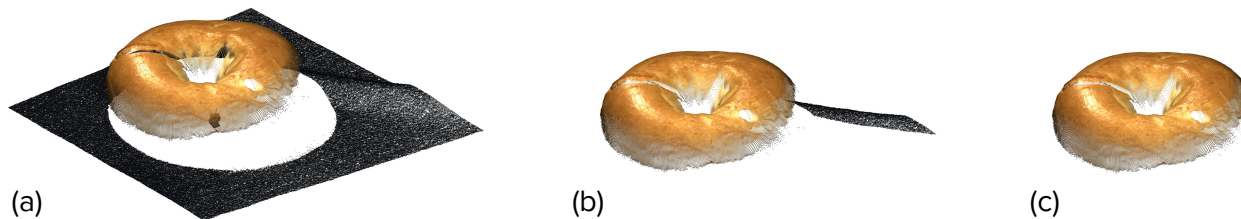


Figure 5: **3D-Aware Preprocessing:** In (a), a "wave" in the fabric is an example of possible background artifacts. Although a RANSAC-based plane removal step approximates the best fitting plane, in some cases, artifacts are too far away from it to be removed (b). To further remove remaining artifacts, DB Scan connected components scanning and removal is used (c).

Following the discussion in Sec. 4.2 on the preprocessing potential, we developed a short preprocessing protocol to handle such cases. First, the background plane is estimated using RANSAC [16] on the 3D locations of image boundary points. Once removed, a connected-components step ensures outliers and areas far from the plane are not kept. This process is illustrated by Fig. 5. A final preprocessing step includes changing the aspect ratio of two nonsquare classes (i.e. *rope* and *tire*). Unless otherwise stated, our results in the paper use this preprocessing pipeline. For a full discussion on the benefits it holds, see Sec. 5. For implementation details see App. C.

Table 5: *Detailed I-ROCAUC Results*: Top half are current state-of-the-art, bottom half are methods investigated by us. A large number of our methods outperform all current methods by a wide margin. "iNet" indicates ImageNet pre-trained

Method	Bagel	Cable Gland	Carrot	Cookie	Dowel	Foam	Peach	Potato	Rope	Tire	Mean	
Previous Methods	Voxel GAN	0.383	0.623	0.474	0.639	0.564	0.409	0.617	0.427	0.663	0.577	0.537
	+ RGB	0.680	0.324	0.565	0.399	0.497	0.482	0.566	0.579	0.601	0.482	0.517
	Voxel AE	0.693	0.425	0.515	0.79	0.494	0.558	0.537	0.484	0.639	0.583	0.571
	+ RGB	0.510	0.540	0.384	0.693	0.446	0.632	0.550	0.494	0.721	0.413	0.538
	Voxel VM	0.75	0.747	0.613	0.738	0.823	0.693	0.679	0.652	0.609	0.69	0.699
	+ RGB	0.553	0.772	0.484	0.701	0.751	0.578	0.480	0.466	0.689	0.611	0.609
	Depth GAN	0.53	0.376	0.607	0.603	0.497	0.484	0.595	0.489	0.536	0.521	0.523
	+ RGB	0.538	0.372	0.580	0.603	0.430	0.534	0.642	0.601	0.443	0.577	0.532
	Depth AE	0.468	0.731	0.497	0.673	0.534	0.417	0.485	0.549	0.564	0.546	0.546
	+ RGB	0.648	0.502	0.650	0.488	0.805	0.522	0.712	0.529	0.540	0.552	0.595
	Depth VM	0.51	0.542	0.469	0.576	0.609	0.699	0.45	0.419	0.668	0.52	0.546
	+ RGB	0.513	0.551	0.477	0.581	0.617	0.716	0.450	0.421	0.598	0.623	0.555
Our Findings	RGB iNet	0.876	0.880	0.791	0.682	0.912	0.701	0.695	0.618	0.841	0.702	0.770
	Depth iNet	0.686	0.532	0.769	0.853	0.857	0.511	0.573	0.620	0.758	0.590	0.675
	NSA	0.841	0.494	0.776	0.913	0.636	0.616	0.795	0.597	0.856	0.438	0.696
	Raw	0.627	0.506	0.599	0.654	0.573	0.531	0.531	0.611	0.412	0.678	0.573
	HoG	0.487	0.588	0.690	0.546	0.643	0.593	0.516	0.584	0.506	0.429	0.559
	SIFT	0.711	0.656	0.892	0.754	0.828	0.686	0.622	0.754	0.767	0.598	0.727
	FPFH	0.825	0.551	0.952	0.797	0.883	0.582	0.758	0.889	0.929	0.653	0.782
	RGB+FPFH	0.918	0.748	0.967	0.883	0.932	0.582	0.896	0.912	0.921	0.886	0.865

5 Discussion

Having conducted an extensive empirical evaluation of 3D representations for AD&S, we can answer the questions raised in the introduction. As a result of the comparison performed in Sec. 4.1 we can conclude that current 3D methods for AD&S do *not* outperform established methods from 2D AD&S. Based on the analysis performed in Sec. 4.2 we can motivate the utility of 3D information, both in regards to the core task of AD&S as well as for secondary tasks such as preprocessing and refinement. The main insight drawn by the extensive evaluation performed in Sec. 4.3 is that for 3D AD&S that utilizes handcrafted representations, *orientation invariance is of utmost importance*. As a result, currently, *handcrafted features surpass learning-based ones*. Last, we point to the fact that by fusing RGB with 3D, one can take the best from both worlds.

We thus conclude with a short list of mini-discussions intended to spark further research in the field of 3D AD&S.

Image-level anomaly detection. While the best performing method that we investigated established a new state-of-the-art on all metrics, the image level detection accuracy is far from perfect. The best performing method reaches an *I-ROC* of 86.5%, a great improvement compared to past methods, but still a relatively low score. As seen in Fig. 3 and Fig. 4, it is not uncommon for methods to perform very well on the segmentation task while underperforming on the detection task. Since we use the PatchCore method as the backbone for most of our experiments, the *I-ROC* score is a function of the test patch most distant from all training patches. However, this assumption was made to address 2D images. It is possible that for multi-modal cases such as 3D and RGB, new assumptions and methods are needed.

Failure classes. As can be seen from Tab. 4, 5, different methods find different classes are harder than others. We highlight two classes for which the simple RGB method outperforms even the best methods. Both *cable gland* and *foam* perform noticeably poorly for all depth-based methods. Although these classes exhibit more RGB-only anomalies compared to others (see Fig. 1), the fusion of both modalities would be expected to handle them. Unfortunately, the fused feature underperformed the RGB only result. This suggests that further research into the feature fusion process is required.

Datasets. While MVTEC 3D-AD is a good starting point for 3D AD&S, its setting is somewhat synthetic. For the field to mature, more datasets are needed. Specifically, due to the complex geometry and interactions of real world scenes, scene level datasets (e.g. [10, 42]) for 3D AD&S may provide a setting where 3D information provides an even greater advantage over 2D counterparts. As LiDAR sensors become cheaper and ever more present (e.g. some iPhone models

Table 6: Preprocessing results, average *PRO/I-ROC* across all classes are reported

	RGB	HoG	SIFT	FPFH
Raw	0.876/0.788	0.625/0.558	0.869/0.723	0.930/0.764
Pre	0.876/0.770	0.771/0.559	0.910/0.727	0.924/0.782

are now equipped with LiDAR sensors), new opportunities for "in the wild" 3D AD&S present themselves e.g. a skin lesion dataset for 3D AD&S. Utilizing 3D information, such datasets could pave the way for early-detection and self-diagnosis AD&S methods against terminal illnesses. Additionally, datasets captured by a variety of methods and 3D formats could improve generalization and robustness.

Methods. We have shown a surface matching descriptor achieved the state-of-the-art results on 3D AD&S tasks. The main reason behind its success is the orientation invariance. While both depth and 3D methods optimize this property, explicit orientation invariance, guided by 3D information can significantly improve the RGB features. An additional exciting future research direction is the adaptation of surface matching ideas to the AD&S setting. Moreover, while our study focused on handcrafted features as a simple and highly effective way to tackle this task, newer, learning-based methods from the surface matching domain are a promising future direction. Another possibility for future research is the finetuning of pre-trained features on the normal training images. Such methods (e.g. MSAD [32]) achieve strong results in the 2D setting.

3D-based preprocessing. As mentioned in Sec. 4.5 and illustrated by Fig. 5, our results are all acquired by using the described preprocessing protocol. It left the RGB method mostly unaffected. More interestingly, it drastically improved results for the depth-based methods, while for 3D-based methods (i.e. FPFH) it slightly decreases results. We postulate this is due to the different ways in which depth and 3D methods handle missing information by the sensor. 3D sensing methods are prone to sampling noise and areas with missing information. In MVTEC 3D-AD it is common to have very noisy backgrounds, these areas are replaced by zeros by the dataset designers. When working with point clouds, these values are all located at the origin and may be ignored by the method as they are not in the spatial context of other points. In contrast, when working with the depth image, these values are in the spatial context of other points. Removing these planes thus helps depth-based methods. We conjecture this is in part the reason for the poor results on depth images reported by the MVTEC 3D-AD baselines and that this preprocessing may improve them. A quantitative comparison is available at Tab. 6

6 Conclusion

We first showed that color-only approaches outperform all existing 3D methods on the MVTEC 3D-AD dataset. We conducted an extensive investigation of 3D representations and found that an orientation-invariant representation achieves the best performance on 3D anomaly detection. Combinations of 3D and color features set a new state-of-the-art. We hope that our work will serve as a strong starting point for future 3D anomaly detection and segmentation approaches.

7 Acknowledgements

This work was supported in part by Oracle Cloud credits and related resources provided by the Oracle for Research program.

References

- [1] Bengs, M., Behrendt, F., Krüger, J., Opfer, R., Schlaefer, A.: Three-dimensional deep learning with spatial erasing for unsupervised anomaly segmentation in brain mri. *International journal of computer assisted radiology and surgery* **16**(9), 1413–1423 (2021) [3](#)
- [2] Bergmann, P., Fauser, M., Sattlegger, D., Steger, C.: Mvtec ad—a comprehensive real-world dataset for unsupervised anomaly detection. In: *Proceedings of the IEEE/CVF conference on computer vision and pattern recognition*. pp. 9592–9600 (2019) [1](#), [4](#)
- [3] Bergmann, P., Fauser, M., Sattlegger, D., Steger, C.: Uninformed students: Student-teacher anomaly detection with discriminative latent embeddings. In: *Proceedings of the IEEE/CVF Conference on Computer Vision and Pattern Recognition*. pp. 4183–4192 (2020) [3](#)
- [4] Bergmann, P., Jin, X., Sattlegger, D., Steger, C.: The mvtec 3d-ad dataset for unsupervised 3d anomaly detection and localization. *arXiv preprint arXiv:2112.09045* (2021) [1](#), [3](#), [4](#), [5](#)
- [5] Bergmann, P., Sattlegger, D.: Anomaly detection in 3d point clouds using deep geometric descriptors. *arXiv preprint arXiv:2202.11660* (2022) [3](#)
- [6] Bergmann, P., Sattlegger, D.: Anomaly detection in 3d point clouds using deep geometric descriptors. *arXiv preprint arXiv:2202.11660* (2022) [5](#)
- [7] Bradley, A.P.: The use of the area under the roc curve in the evaluation of machine learning algorithms. *Pattern recognition* **30**(7), 1145–1159 (1997) [4](#)
- [8] Chen, T., Kornblith, S., Norouzi, M., Hinton, G.: A simple framework for contrastive learning of visual representations. *arXiv preprint arXiv:2002.05709* (2020) [3](#)
- [9] Cohen, N., Hoshen, Y.: Sub-image anomaly detection with deep pyramid correspondences. *arXiv preprint arXiv:2005.02357* (2020) [1](#), [3](#), [6](#)
- [10] Dai, A., Chang, A.X., Savva, M., Halber, M., Funkhouser, T., Nießner, M.: Scannet: Richly-annotated 3d reconstructions of indoor scenes. In: *Proceedings of the IEEE conference on computer vision and pattern recognition*. pp. 5828–5839 (2017) [9](#)
- [11] Dalal, N., Triggs, B.: Histograms of oriented gradients for human detection. In: *2005 IEEE computer society conference on computer vision and pattern recognition (CVPR’05)*. vol. 1, pp. 886–893. Ieee (2005) [7](#)
- [12] Defard, T., Setkov, A., Loesch, A., Audigier, R.: Padim: a patch distribution modeling framework for anomaly detection and localization. In: *International Conference on Pattern Recognition*. pp. 475–489. Springer (2021) [3](#)
- [13] Deng, J., Dong, W., Socher, R., Li, L.J., Li, K., Fei-Fei, L.: Imagenet: A large-scale hierarchical image database. In: *2009 IEEE conference on computer vision and pattern recognition*. pp. 248–255. Ieee (2009) [5](#), [14](#)
- [14] Eskin, E., Arnold, A., Prerau, M., Portnoy, L., Stolfo, S.: A geometric framework for unsupervised anomaly detection. In: *Applications of data mining in computer security*, pp. 77–101. Springer (2002) [3](#)
- [15] Ester, M., Kriegel, H.P., Sander, J., Xu, X., et al.: A density-based algorithm for discovering clusters in large spatial databases with noise. In: *KDD* (1996) [15](#)
- [16] Fischler, M.A., Bolles, R.C.: Random sample consensus: a paradigm for model fitting with applications to image analysis and automated cartography. *Communications of the ACM* **24**(6), 381–395 (1981) [8](#), [15](#)
- [17] Gidaris, S., Singh, P., Komodakis, N.: Unsupervised representation learning by predicting image rotations. *arXiv preprint arXiv:1803.07728* (2018) [3](#)
- [18] Glodek, M., Schels, M., Schwenker, F.: Ensemble gaussian mixture models for probability density estimation. *Computational Statistics* **28**(1), 127–138 (2013) [3](#)
- [19] Golan, I., El-Yaniv, R.: Deep anomaly detection using geometric transformations. In: *NeurIPS* (2018) [3](#)
- [20] He, K., Fan, H., Wu, Y., Xie, S., Girshick, R.: Momentum contrast for unsupervised visual representation learning. *arXiv preprint arXiv:1911.05722* (2019) [3](#)
- [21] He, K., Fan, H., Wu, Y., Xie, S., Girshick, R.: Momentum contrast for unsupervised visual representation learning. In: *Proceedings of the IEEE/CVF Conference on Computer Vision and Pattern Recognition*. pp. 9729–9738 (2020) [3](#)
- [22] Hendrycks, D., Mazeika, M., Kadavath, S., Song, D.: Using self-supervised learning can improve model robustness and uncertainty. In: *NeurIPS* (2019) [3](#)
- [23] Jolliffe, I.: *Principal component analysis*. Springer (2011) [3](#)

- [24] Klaser, A., Marszalek, M., Schmid, C.: A spatio-temporal descriptor based on 3d-gradients. In: BMVC 2008-19th British Machine Vision Conference. pp. 275–1. British Machine Vision Association (2008) 7
- [25] Latecki, L.J., Lazarevic, A., Pokrajac, D.: Outlier detection with kernel density functions. In: International Workshop on Machine Learning and Data Mining in Pattern Recognition. pp. 61–75. Springer (2007) 3
- [26] Li, C.L., Sohn, K., Yoon, J., Pfister, T.: Cutpaste: Self-supervised learning for anomaly detection and localization. In: Proceedings of the IEEE/CVF Conference on Computer Vision and Pattern Recognition. pp. 9664–9674 (2021) 3, 6, 14
- [27] Liu, F.T., Ting, K.M., Zhou, Z.H.: Isolation forest. In: 2008 Eighth IEEE International Conference on Data Mining. pp. 413–422. IEEE (2008) 3
- [28] Lowe, D.G.: Distinctive image features from scale-invariant keypoints. *International journal of computer vision* **60**(2), 91–110 (2004) 7
- [29] Perera, P., Patel, V.M.: Learning deep features for one-class classification. *IEEE Transactions on Image Processing* **28**(11), 5450–5463 (2019) 3
- [30] Pérez, P., Gangnet, M., Blake, A.: Poisson image editing. *SIGGRAPH* (2003) 6, 14
- [31] Reiss, T., Cohen, N., Bergman, L., Hoshen, Y.: Panda: Adapting pretrained features for anomaly detection and segmentation. In: Proceedings of the IEEE/CVF Conference on Computer Vision and Pattern Recognition. pp. 2806–2814 (2021) 3, 6
- [32] Reiss, T., Hoshen, Y.: Mean-shifted contrastive loss for anomaly detection. *arXiv preprint arXiv:2106.03844* (2021) 10
- [33] Roth, K., Pemula, L., Zepeda, J., Schölkopf, B., Brox, T., Gehler, P.: Towards total recall in industrial anomaly detection. *arXiv preprint arXiv:2106.08265* (2021) 1, 3, 5
- [34] Ruff, L., Gornitz, N., Deecke, L., Siddiqui, S.A., Vandermeulen, R., Binder, A., Müller, E., Kloft, M.: Deep one-class classification. In: *ICML* (2018) 3
- [35] Rusu, R.B., Blodow, N., Beetz, M.: Fast point feature histograms (fpfh) for 3d registration. In: 2009 IEEE International Conference on Robotics and Automation. pp. 3212–3217 (2009). <https://doi.org/10.1109/ROBOT.2009.5152473> 7
- [36] Schlegl, T., Seeböck, P., Waldstein, S.M., Langs, G., Schmidt-Erfurth, U.: f-anogan: Fast unsupervised anomaly detection with generative adversarial networks. *Medical image analysis* **54**, 30–44 (2019) 3
- [37] Schlegl, T., Seeböck, P., Waldstein, S.M., Schmidt-Erfurth, U., Langs, G.: Unsupervised anomaly detection with generative adversarial networks to guide marker discovery. In: *International Conference on Information Processing in Medical Imaging* (2017) 1, 3
- [38] Schlüter, H.M., Tan, J., Hou, B., Kainz, B.: Self-supervised out-of-distribution detection and localization with natural synthetic anomalies (nsa). *arXiv preprint arXiv:2109.15222* (2021) 3, 6, 14
- [39] Scholkopf, B., Williamson, R.C., Smola, A.J., Shawe-Taylor, J., Platt, J.C.: Support vector method for novelty detection. In: *NIPS* (2000) 3
- [40] Scovanner, P., Ali, S., Shah, M.: A 3-dimensional sift descriptor and its application to action recognition. In: Proceedings of the 15th ACM international conference on Multimedia. pp. 357–360 (2007) 7
- [41] Simarro Viana, J., de la Rosa, E., Vande Vyvere, T., Robben, D., Sima, D.M., et al.: Unsupervised 3d brain anomaly detection. In: *International MICCAI Brainlesion Workshop*. pp. 133–142. Springer (2020) 3
- [42] Song, S., Lichtenberg, S.P., Xiao, J.: Sun rgb-d: A rgb-d scene understanding benchmark suite. In: Proceedings of the IEEE conference on computer vision and pattern recognition. pp. 567–576 (2015) 9
- [43] Tack, J., Mo, S., Jeong, J., Shin, J.: Csi: Novelty detection via contrastive learning on distributionally shifted instances. *arXiv preprint arXiv:2007.08176* (2020) 3
- [44] Wu, Z., Song, S., Khosla, A., Yu, F., Zhang, L., Tang, X., Xiao, J.: 3d shapenets: A deep representation for volumetric shapes. In: Proceedings of the IEEE conference on computer vision and pattern recognition. pp. 1912–1920 (2015) 5
- [45] Yu, J., Zheng, Y., Wang, X., Li, W., Wu, Y., Zhao, R., Wu, L.: Fastflow: Unsupervised anomaly detection and localization via 2d normalizing flows. *arXiv preprint arXiv:2111.07677* (2021) 3
- [46] Zagoruyko, S., Komodakis, N.: Wide residual networks. *arXiv preprint arXiv:1605.07146* (2016) 14
- [47] Zhou, Q.Y., Park, J., Koltun, V.: Open3D: A modern library for 3D data processing. *arXiv:1801.09847* (2018) 15

- [48] Zong, B., Song, Q., Min, M.R., Cheng, W., Lumezanu, C., Cho, D., Chen, H.: Deep autoencoding gaussian mixture model for unsupervised anomaly detection. ICLR (2018) [3](#)

A Detailed P-ROC Results

Detailed P-ROC Results: Results not reported for previous methods, "iNet" indicates ImageNet pre-trained

Method	Bagel	Cable Gland	Carrot	Cookie	Dowel	Foam	Peach	Potato	Rope	Tire	Mean
RGB iNet	0.983	0.984	0.980	0.974	0.972	0.849	0.976	0.983	0.987	0.977	0.967
Depth iNet	0.959	0.896	0.966	0.969	0.967	0.743	0.969	0.958	0.977	0.888	0.930
NSA	0.925	0.638	0.872	0.908	0.674	0.777	0.902	0.825	0.972	0.676	0.817
Raw Depth	0.803	0.747	0.848	0.801	0.610	0.694	0.829	0.770	0.950	0.657	0.771
HoG	0.912	0.933	0.985	0.826	0.936	0.857	0.923	0.987	0.980	0.955	0.930
SIFT	0.986	0.956	0.996	0.952	0.966	0.919	0.985	0.997	0.993	0.983	0.974
FPFH	0.994	0.966	0.999	0.946	0.966	0.927	0.996	0.999	0.996	0.990	0.978
RGB+FPFH	0.996	0.992	0.997	0.994	0.981	0.974	0.996	0.998	0.994	0.995	0.992

B Method Specific Implementation Details

Bellow, we present additional implementation details for each of our investigated methods

B.1 RGB-only ImageNet Features

Utilizing PatchCore, RGB images are fed into an ImageNet [13] pre-trained WideResNet50 [46] backbone as a feature extractor. To allow for localized segmentation, patch-level features are extracted from the aggregated outputs of blocks 2 and 3, resulting in a feature dimension of 1536.

B.2 Depth-only ImageNet Features

As in the RGB-only case, PatchCore is used with a depth map normalized according to ImageNet statistics.

B.3 Raw Depth Values

The depth image is divided into patches of 8×8 pixels, resulting in 28×28 patches. The descriptor is comprised of the 8×8 pixels of each patch, flattened to a 1D list of length 64.

B.4 NSA

We were not able to find an official implementation of CutPaste [26] and the public unofficial implementations lag behind the reported figures by up to 10%. Therefore, we compare our method to NSA [38], a follow-up to CutPaste that uses Poisson blending [30] to achieve more realistic augmentations. To test NSA on the new dataset, we modified their official implementation to handle depth images. The current implementation requires the images to be represented as integers, as such, the depth images are discretized to $[0, 255]$. Furthermore, NSA uses extensive, class-dependent hyperparameters. MVTec 3D-AD classes were assigned hyperparameters by visually comparing them with the original classes and assigning the values of the most similar class. Depth images are used for running these experiments.

B.5 HoG

The depth image is used as an input. To align with the feature map resolution, 8 pixels per cell, and 1 cell per block are used. 8 bins are used to arrive at a 32 dimensional representation.

B.6 D-SIFT

The depth image is used as an input. Dense SIFT is applied to all the pixels, to reduce the resolution, average pooling is applied. Following standard SIFT practice, a 128 feature dimension is used.

B.7 FPFH

To speed up calculations of FPFH, the point cloud is downsampled prior to running the algorithm. The downsampling is performed on the organized point cloud (i.e. image downsampling). It is then flattened into an unorganized point cloud. Using the implementation from the open-source library Open3D [47], a descriptor is extracted for each point. These descriptors are then reshaped back into an organized point cloud and their resolution is lowered by average pooling them. FPFH requires normals to run, we estimate the normals using Open3D. The radius for the FPFH algorithm is 0.25 and the *max_nn* parameter is set to 100. The resulting feature is of dimension 33.

C Preprocessing Implementation Details

C.1 Plane Removal

By design, the objects in the dataset are centered within the image. We thus make a simplifying assumption that all the edges of the image lie on the same plane. To this end, a 10 pixels wide strip around the image boundary is taken from the organized point cloud. After removing all NaNs (i.e. noise), RANSAC [16] is used to approximate the plane that best describes the boundary. The distance to this plane is calculated for each point in the point cloud, any point within 0.005 distance is removed. In practice, instead of removing the point, we zero the XYZ coordinates and RGB values for the point. This ensures the original resolution is kept. We use the Open3D [47] "Segment Plane" implementations for the RANSAC step with *ransac_n* = 50 and *num_iterations* = 1000, for the actual plane removal we use the returned plane equation and manually zero the values.

C.2 Clustering Based Outlier Removal

Although the plane removal step can identify and remove the majority of the planes, in some cases, the planes are not planar, see Fig 5. Points in those areas may therefore be flagged as anomalies. By running DB-Scan [15] as a connected-components approach, each cluster is treated as a connected component. We keep the largest component and remove all points from other components (as before, we zero the XYZ coordinates and RGB values of the point). We use the Open3D [47] DB-Scan implementation with $\epsilon = 0.006$ and *min_points* = 30.